Modeling the Interaction of the NIF Laser Beam with Laser Components

M. D. Feit

C. D. Boley

Large laser systems with high peak power, such as the National Ignition Facility (NIF), contain a great variety of optical components. These include lenses, mirrors, potassium dihydrogen phosphate (KDP) crystals, spatial filters, diffractive optics plates, debris shields, and so forth. The NIF beam has sufficient intensity to produce adverse effects either on these components themselves or on their functionality as part of the laser. Laser-interaction modeling like that normally used in treating ICF targets plays an important role in ameliorating these adverse effects.

We illustrate such modeling here with two examples. These arise from the need to avoid pinhole closure in the spatial filters and the need to avoid laser-induced damage to optical elements such as lenses.

Spatial filters remove high spatial frequency noise from the beam[1] by focusing it through a pinhole. The material forming the pinhole removes the most divergent rays, which are found at the outermost part of the focused beam. At NIF intensities (see below), the laser intensity at the pinhole edge can be sufficiently large to create a plasma that can expand into the pinhole and degrade the quality of light passing through the pinhole later in the pulse. This degradation, called pinhole closure, is examined below for various pinhole designs.

To contain cost, large laser systems like NIF necessarily operate near laser-induced damage thresholds for some optical elements. On the other hand, because of the very large number of components, it is necessary to establish safe operational limits and tolerable levels of damage risk. It would be difficult to establish such limits from experimentation alone because of the large number of materials, coatings, and environments, and the need to scale from results of small-scale experiments to full-sized optical elements. Thus, it is useful to establish theoretical models of laser-induced damage to aid understanding, interpretation, and application of empirical results; for example, there exists a good understanding of the deleterious effects of intensification due to nonlinear propagation (self-focusing).[2] In this article, we discuss mechanisms of laser damage initiation on fused silica. (Except for the frequency-doubling and -tripling crystals, all optics in the NIF Final Optics Assembly will be fabricated from fused silica.) The results presented here are part of an extensive experimental-theoretical effort to understand 3ω fused silica damage, in order to ameliorate it and to devise quality assurance tests of damage vulnerability suitable for NIF.[3] This 3ω fused-silica laser damage effort, led by M. R. Kozlowski, has been documented in numerous Boulder Damage Symposium papers during the past few years.

Pinhole Modeling

In a spatial filter, a pinhole subtending a half-angle α removes incoming rays misdirected beyond this angle, as illustrated schematically in Figure 1. Equivalently,

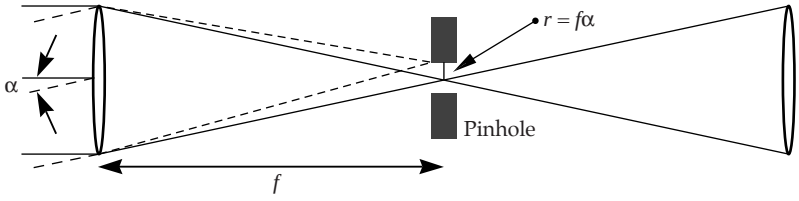

FIGURE 1. Schematic geometry of a spatial filter (not to scale), showing incoming rays misdirected by a given angle brought to a common point in the focal plane.
(70-00-0499-0960-pb01)

the pinhole removes noise of spatial wavelength shorter than λ/α. If the angle is too small, however, the wings of the beam at focus can deposit substantial energy on the pinhole material.[4] For typical NIF pulses, the intensities near the pinhole edge will range from several GW/cm^2 to several TW/cm^2, depending on the pinhole size, the pulse shape, and the beam alignment. At these intensities, the material will generate a plasma that expands into the pinhole and that can cause difficulties. At lower electron densities, the plasma will induce aberrations on the beam, while at higher electron densities, the plasma will deflect and absorb the beam.

We have modeled two types of pinholes, shown in Figure 2. The first type, which we have treated more extensively than the second, consists of four azimuthally spaced blades, staggered in the longitudinal direction (parallel to the beam), with the blades successively rotated by 90°. The use of staggered blades avoids plasma convergence at the centerline, in contrast to a circular "washer" type pinhole. The longitudinal separation of adjacent blades (typically 2.4 mm) is sufficient to minimize interactions among the plasmas during the passage of the beam. At the same time, the blades are close enough so that each filters the beam in the far field. This is possible because an aberrated beam has an extended range near focus. The blades can be situated either horizontally/vertically ("square" orientation) or at a 45° angle ("diamond" orientation) relative to the far-field pattern of the square laser beam. The latter orientation performs better than the former, because it allows more room for the diffractive lobes of the beam at focus, which extend horizontally and vertically from the central spot.

The second type of pinhole has a conical shape, which is designed to refract the filtered light away from the beam rather than to absorb it.[5] Experiments have shown that this design is superior to the blade design.[6] Cones pass at least twice the energy of blades, and they also avoid a back reflection problem encountered with blades. However, they are more difficult to model than blades. One reason is that their longitudinal length is 3 to 4 times that of the blade design, with the result that the intensity distribution at the entrance differs significantly from that at focus. In the work described here, cones are treated via a comparatively primitive model, which also applies to blades.

FIGURE 2. Typical 4-leaf and cone pinholes. The size of the square opening in this 4-leaf pinhole is 2.7 mm.
(70-00-0499-0961pb01)

We expect the fourth-pass pinhole in the NIF cavity spatial filter (CSF) to present the greatest problems. To compare this with the pinhole on the NIF transport spatial filter (TSF), we employ simple scaling arguments.[6] Assuming that the plasma closure speed is constant, one can show that the closure time is sensitive to the *f*-number of the spatial filter, scaling approximately as f^3, and that it also scales roughly with the inverse of the beam power. On NIF, the CSF and TSF have *f*-numbers of 31 and 80, respectively, while the power into the TSF is at most three times that into the fourth pass of the CSF. Applying the anticipated scaling, we expect the fourth-pass CSF pinhole to have a closure time about 1/6 that of the TSF pinhole. The former pinhole, therefore, should present more serious problems than any other NIF pinhole. Its behavior was simulated by experiments on Beamlet, which has two spatial filters of *f*-number 26, close to the value of the NIF CSF. The Beamlet TSF was chosen because of its higher beam power and its proximity to output diagnostics. The pinhole experiments were performed during 1997 and 1998 (Ref. 6).

In addition to experiments on Beamlet, pinhole-related experiments were conducted with the Optical Sciences Laser (OSL)[7] to understand the dependence of plasma speed on irradiance and material composition. Here a blade was illuminated with a pulse of intensity similar to that expected on pinhole edges, and the electron density of the ablated plasma was probed in time via interferometry. This allowed for the study of phenomena in an off-line setting. We used the results to explore parameter dependencies and to test our numerical models.

In the following discussion, we consider first the OSL experiments and then the Beamlet experiments.

Modeling OSL Experiments

In the OSL experiments,[7] a strong pulse of peak intensity 50–600 GW/cm^2 and duration 5 to 15 ns struck a material blade (knife edge) at a right angle. The materials of interest for pinholes were stainless steel and tantalum (Ta). These were chosen because we found that high-Z materials generally exhibit slower closure rates than low-Z materials. The geometry is illustrated in Figure 3. A probe beam was passed over the blade and through the main beam, and its phase shift was measured as a function of distance above the blade and time. In modeling this experiment,[8] we set up the two beams and the blade, with many thin zones near the surface of the blade. These zones, which followed the material, expanded into the vacuum as the material vaporized.

To describe the plasma, we employed LASNEX, a 2D Lagrangian radiation hydrodynamics code typically used in ICF

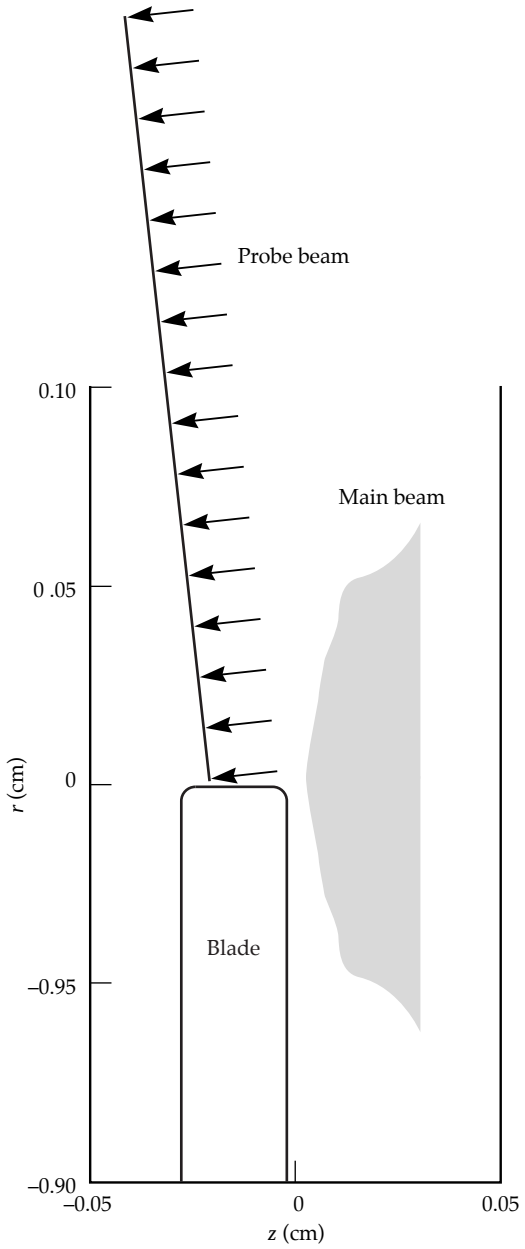

FIGURE 3. Schematic illustration of knife-edge experiments on OSL. The intensity profile of the main beam is indicated. Both this beam and the probe beam have circular profiles. (70-00-0499-0962pb01)

target calculations.[9,10] LASNEX calculates the absorption and refraction of the rays and the plasma properties. While it is believed to be the best available code for the present purposes, this application represents a low-energy extrapolation of its normal range. The code does not treat in detail, for example, the thermodynamics of vaporization. Of primary interest here is the electron density, which produces phase shifts in the probe beam by decreasing the local index of refraction according to

$$n(\mathbf{x}) = \left[1 - n_e(\mathbf{x}) / n_c\right]^{1/2} , \quad (1)$$

where n_c is the critical density (about 10^{21} cm^{-3} for light of wavelength 1053 nm). The optical path difference in waves along a ray path is proportional to the line integral of the change in the index of refraction:

$$\phi = -\int (n-1)\frac{dl}{\lambda} , \quad (2)$$

with the sign chosen to make ϕ positive.

Figure 4 shows typical LASNEX predictions for the electron density midway through a pulse of maximum intensity 175 GW/cm^2, incident on a Ta blade. Note that the expansion is nearly symmetrical about the tip of the blade. The electron density decreases almost exponentially with distance, with the critical electron density located a few micrometers from the surface. The maximum electron temperature is about 40 eV, while the maximum ionization state is about 19. Each of these quantities is moderately uniform within the bulk plasma but decreases sharply near the blade.

To find the phase change of the probe beam, we employed the postprocessing code HOLOX.[11] For typical plasma sizes at the midpoint of a pulse, an electron density of about 10^{18} cm^{-3} produced a shift of a single wave with insignificant deflection. Note that this is three orders of magnitude below the critical density.

In both experiment and simulation, the phase profile exhibited a regular behavior as a function of distance above the blade and time. At a given time, the phase decreased exponentially with distance above the blade. As time increased, the phase profiles flattened out in a regular manner. This is illustrated in Figure 5, which shows the phase profiles at particular times for a stainless-steel blade, which we model as iron. Note that the calculated phase change generally

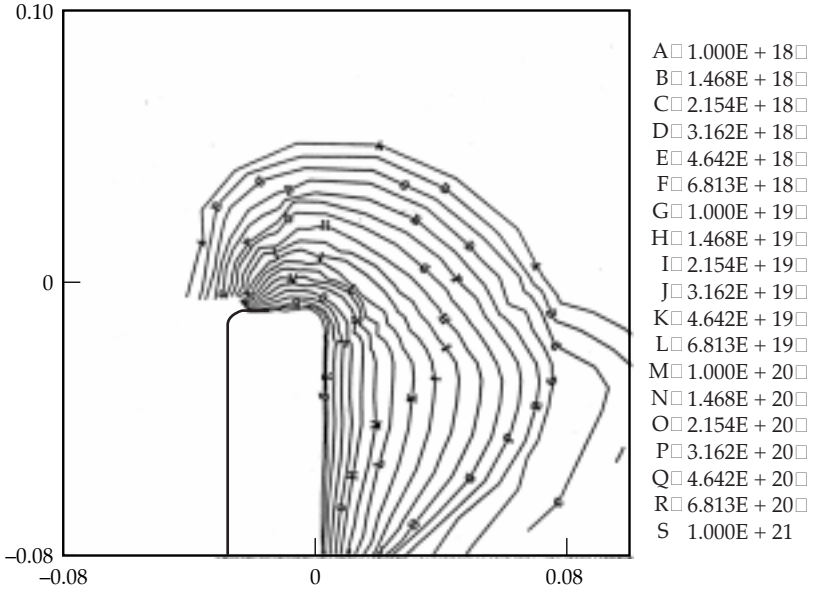

FIGURE 4. Electron density at t = 10 ns, for a pulse of maximum intensity 175 GW/cm^2 on a Ta blade on OSL, as calculated by LASNEX. The contour labels give the electron density in cm^{-3}. Dimensions are in cm. (70-00-0499-0963pb01)

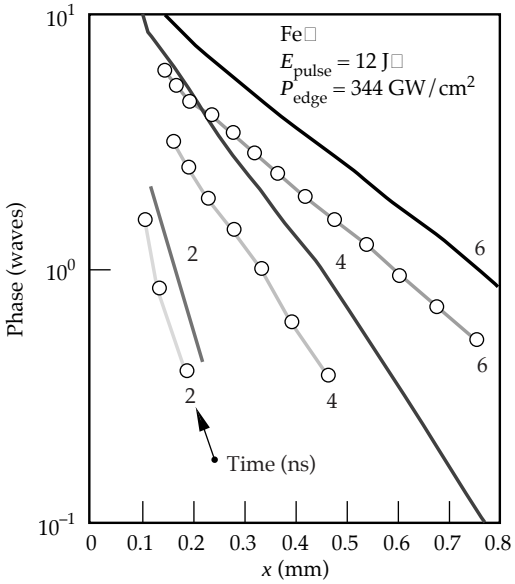

FIGURE 5. Phase profiles versus distance from the blade, for a pulse of peak intensity 345 GW/cm^2 illuminating a stainless-steel blade on OSL. The points denote measurements, while the lines give calculations. (70-00-0499-0964pb01)

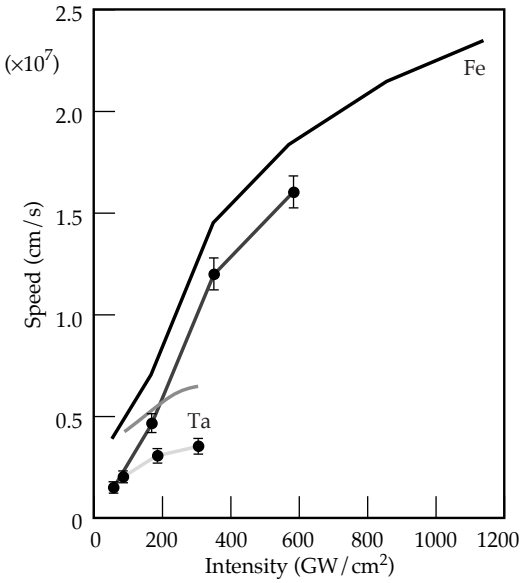

FIGURE 6. Speed of the 1-wave contour on OSL, for blades of stainless steel and Ta. The points denote measurements, while the lines give calculations. (70-00-0499-0965pb01)

exceeds the measured phase change, but that the trends are similar. For both experiment and model, the overall behavior is summarized by a function of the form

$$\phi(x,t) = \exp\frac{c_1(t-t_0)-x}{c_0(t-t_0)}\ , \qquad (3)$$

where x is the distance above the blade. The parameters depend on intensity and material. This functional form is valid for times greater than t_0, the time required for the electron density to reach an exponential profile, which typically is a few nanoseconds. Setting the numerator to zero, we see that c_1 is the "1-wave speed" (the speed of the point with $\phi = 1$). The speed c_0 is related to the rate at which the profiles flatten with respect to position. We always have $c_1 > c_0$. The speed of the nth wave is $c_1 - c_0 \ln n$ (valid as long as it is positive, which typically holds for $n \le 10$).

Figure 6 shows the calculated and measured 1-wave speeds for a range of edge irradiances. For stainless steel, the calculated speed reaches approximately 2.3×10^7 cm/s at 1200 GW/cm^2. This exceeds experiment by a constant offset of about 0.2×10^7 cm/s. The data for Ta cover a more limited range of intensities, reaching only 300 GW/cm^2, and the speeds are smaller because of the larger atomic weight. Again the calculated speeds exceed experiment by a fixed offset. Because of the offsets, the calculated speeds do not appear to aim toward zero at low intensities, which is clearly nonphysical. Indeed, LASNEX was not intended to model this regime.

From the OSL experiments, we learned that the plasma model gives results of about the right magnitude. Although the calculated phase speeds exceed experiment, they do so in a systematic way. Thus the model is conservative, in the sense that it overstates the plasma effects.

Modeling Beamlet Experiments

We extended the plasma calculations to 4-leaf pinholes,[8] using a beam profile appropriate to Beamlet. Since the far-field range of the beam exceeded the longitudinal

length of the pinhole, the plasma calculated for a single blade was replicated and rotated to describe four blades. For a given pinhole size, the electron density in the square orientation was markedly more peaked than that in the diamond orientation, because the far-field lobes intercepted the blades at a higher power level.

To find the effects on the beam, a separate propagation calculation was necessary. We propagated a beam through the entire spatial filter, including the plasmas, via the code PROPN1 (Ref. 12). The plasmas were used to set up phase screens for the code, and the edge of each blade defined a transmission mask. While this scheme should be iterated, the first iteration gave interesting and useful results.

Figure 7 shows lineouts of the calculated near fields, at the image plane located a distance twice the focal length from the output lens, for a Ta pinhole of half-angle 100 μrad in the square orientation. The calculation is for a 20-ns pulse of energy 1 kJ. One sees that the high-frequency noise visible on the incoming wavefront is indeed removed for early time slices (less than 10 ns), when the blades filter the beam without generating significant plasmas. The intensity has been filtered to the expected scale of $\lambda/\alpha \sim 1$ cm. For later time slices, though, the beam breaks up into successively larger regions, and the beam contrast (the normalized variance of the intensity) steadily increases. The characteristic size of the regions also increases, reaching about 5 cm at 19 ns. This trend is also seen in experiment. Closure, defined as a 20% increase in contrast, was observed at about 10 ns, which is close to the calculated time of 11 ns.

When calculations are done for this pinhole in the diamond orientation, however, the pinhole remains open. Such a trend would be expected from the considerations given earlier. In experiment, the pinhole also remaind open at this energy. It finally closed for a pulse of energy between 2 and 3 kJ.

If Ta is replaced by stainless steel, then the diamond pinhole is predicted to close rapidly after 10 ns, in about the same manner as the Ta square orientation. The contrast rises by an order of magnitude between 10 ns and 19 ns. The reason for the adverse behavior is the increased plasma speed. Experimentally, stainless steel also was observed to close more rapidly than Ta.

Although the calculations for 4-leaf pinholes are instructive and reveal trends similar to experiment, they are not readily extended to cone pinholes. In addition, we are interested in describing misalignment effects, for which the plasma and propagation calculations are even more burdensome than those described above. Hence a simple pinhole model has been devised that applies to both 4-leaf and cone pinholes and that can also describe misalignment.[6] The model was developed wth

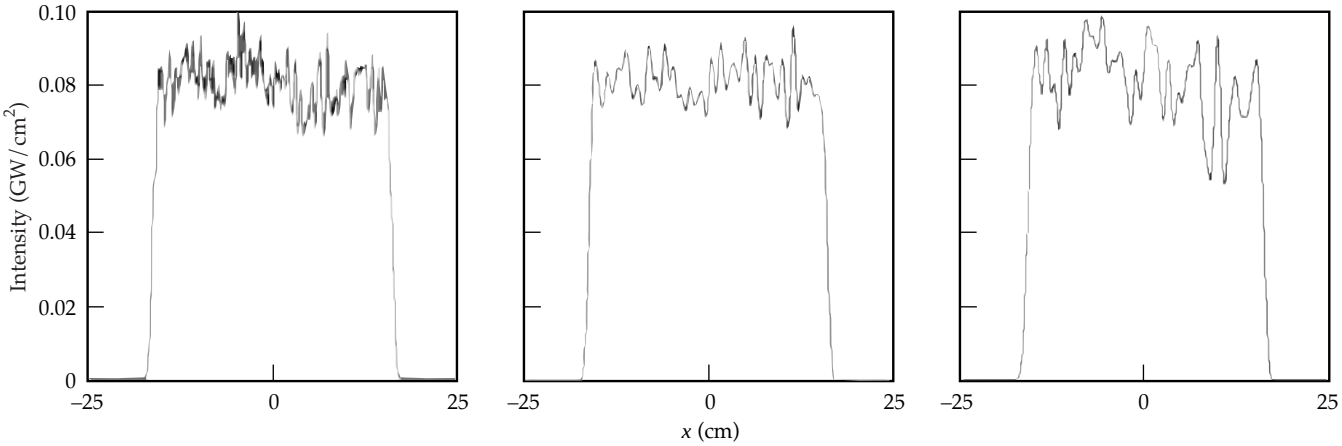

FIGURE 7. Horizontal lineouts, along the beam center, of the calculated near field for a 100-μrad Ta pinhole, in the square orientation. The pulse duration is 20 ns, and the beam energy is 1 kJ. The lineouts give the incoming pulse (left) and the outgoing pulse at 8 ns (center) and 13 ns (right). The horizontal dimension is in cm. (70-00-0499-0966pb01)

J. E. Murray. A schematic view of the focal plane, as pictured in the simple model, is shown in Figure 8. We envision a round beam within a round pinhole, with the center of the beam displaced a distance $r_{mis} = f\alpha$ from the center of the pinhole, where f is the focal length and α is the misalignment angle. The radius r_b of the beam is arbitrarily chosen to enclose 99% of the azimuthally averaged energy. To apply the model to a 4-leaf pinhole, we choose an effective pinhole radius. For the square orientation, this is the pinhole half-width, while for the diamond orientation it is the average distance of a blade from the beam center.

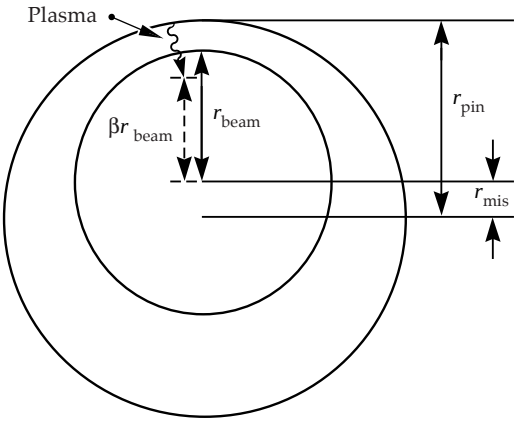

FIGURE 8. Schematic geometry of beam and pinhole, as envisioned in the model of Eq. (4).
(70-00-0499-0967pb01)

We suppose that the pinhole closes when the plasma ablated from the nearest edge, traveling at a particular speed, penetrates to a fraction β of the beam radius. The choice of this speed is somewhat arbitrary. It might seem reasonable to choose the 1-wave speed, but the model works more satisfactorily with a faster speed, corresponding to a smaller wave index. In practice, we have chosen the 0.1-wave speed. From these assumptions, we can write the closure time in the form

$$\tau = \frac{r_{pin} - r_{mis} - \beta r_b}{\gamma c_n \left[I\left(r_{pin} - r_{mis}\right)\right]}, \qquad (4)$$

with r_{pin} the pinhole radius. In the denominator, note that the speed c_n depends on the intensity, which in turn depends on the pinhole radius and misalignment. The dependence of speed on intensity was obtained from OSL measurements, as described above, supplemented with LASNEX results. Since the speed is not known for the glancing angle appropriate to a cone pinhole, we assume that it is the 90° speed, multiplied by a parameter γ. Thus the model has two parameters: β and γ (with $\gamma = 1$ for a 4-leaf pinhole).

Figure 9 shows the closure predictions for a diamond Ta pinhole of half-angle 100 μrad. The upper and lower lines correspond to beam powers of 135 GW and 160 GW, respectively, for a temporally constant pulse shape. The closure time decreases with misalignment, with the sharpest rate of decrease occurring for the smallest misalignment. Also shown are three data points from the Beamlet TSF, with powers in the range 135 to 160 GW. These closure times decrease from 20 ns at 2.5 μrad to about 13 ns near 12 μrad, although the error bars are appreciable. The model matches this behavior and predicts a closure time of about 7 ns at a misalignment of 20 μrad. In the fit we use $\beta = 0.9$, which follows from a fit to all data for 4-leaf pinholes.

Closure times for the stainless-steel cone, of half-angle 100 μrad, are displayed in Figure 10. The lines give predictions for beam powers of 140 GW and 195 GW, with $\beta = 0.9$ and $\gamma = 0.1$. The data are

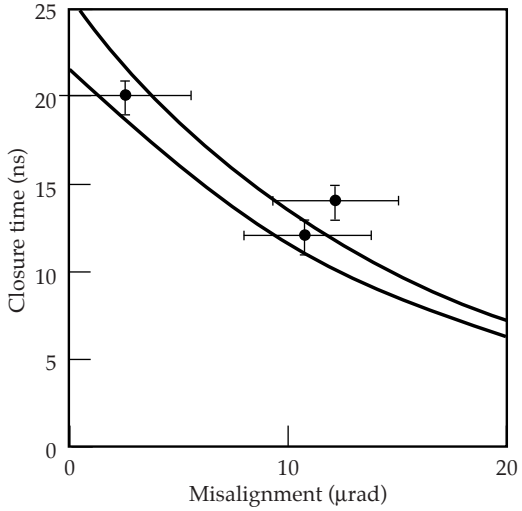

FIGURE 9. Closure time vs misalignment for a diamond Ta pinhole of half-angle 100 μrad, according to model and Beamlet experiment, for a beam power in the range 135–160 GW. The pulse is constant in time. Since the experimental points vary somewhat in beam power, the model curves are given for the largest and smallest powers.
(70-00-0499-0968pb01)

distributed within this range. As in the previous case, the calculated closure time decreases most rapidly at small alignments. Again the model is comparable with experiment, although it is unfortunate that the data tend to congregate near a common point. Additional data would be desirable to test the model more generally.

Finally, we use the model to predict closure as a function of both pinhole size and misalignment for a stainless-steel cone pinhole. Here we attempt to simulate a temporally shaped ignition pulse (Haan pulse) of 14.8 kJ on NIF. On Beamlet, a Haan pulse of 8.3 kJ was observed to close (i.e., barely pass) at 20 ns. For the same misalignment, a temporally flat pulse closed at 2.2 kJ. Assuming simple scaling, we suppose that a 14.8-kJ Haan pulse can be simulated by a flat pulse of 3.9 kJ. Figure 11 shows how the closure time increases as the pinhole half-angle is increased from 100 to 150 μrad. With no misalignment, closure occurs after 20 ns (the point is barely visible in the corner). NIF specifications allow for 10% misalignment, based on the pinhole radius. The calculation indicates that a 120-μrad pinhole provides ample margin for a closure time of 20 ns. In this case, the edge power is 34 GW/cm^2. On the basis of experiments and this modeling, the current NIF design calls for a 150-μrad stainless-steel cone pinhole.

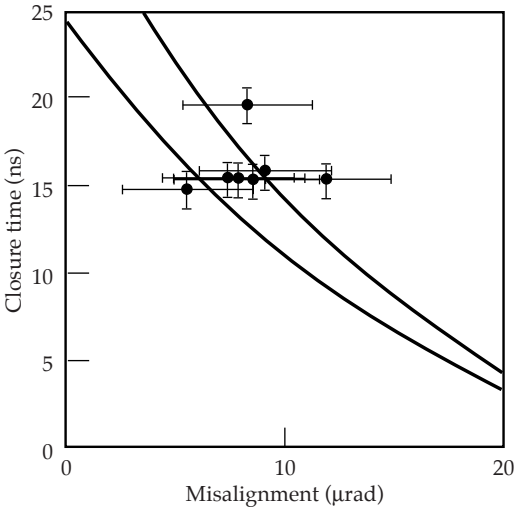

FIGURE 10. Closure time versus misalignment for a stainless-steel cone of half-angle 100 μrad, according to model and Beamlet experiment. The beam power is in the range 140 to 195 GW. (70-00-0499-0969pb01)

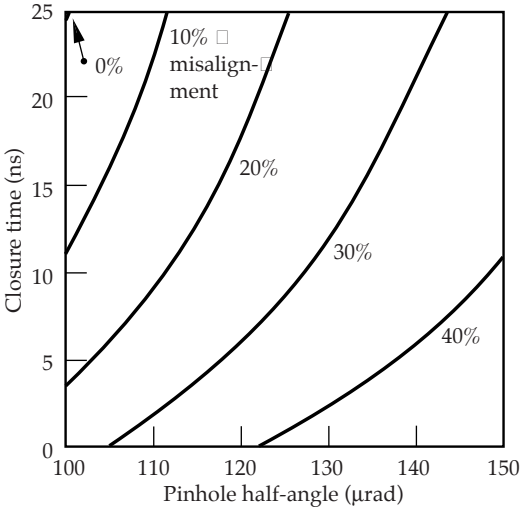

FIGURE 11. Calculated closure time versus pinhole half-angle, as calculated for various fractional misalignments, for a stainless-steel cone. The closure time for a 100-μrad pinhole with perfect alignment is about 25 ns. The pulse simulates a 14.8-kJ ignition pulse. (70-00-0499-0970pb01)

Initiation of Surface Laser Damage

The NIF final optics will operate at a wavelength of 351 nm (3ω or third harmonic of 1-μm light). Optical damage at 3ω is a more severe problem than at first-harmonic wavelength. Damage in fused silica is typically initiated on the surface or in a near-surface layer, usually most visible on the exit side of the optical element for reasons discussed below. Experiments indicate that damage is initiated at subwavelength-sized sites. Local heating of absorbing nanoparticles can result in material fracture due to thermal-induced stress. Also thermal explosion, in which the absorbing region grows in size with heating, can play a role. Damage in fused silica due to bulk defects, e.g., bubbles or inclusions, can also occur but is expected to be ultimately less significant than surface damage because these defects are expected to be relatively rare.

This section discusses our effort to understand quantitatively the interaction of high-power lasers with damage-initiating defects. Our theoretical description must include optical propagation, absorption and ionization of material, hydrodynamics and shock wave propagation, thermal and radiation transport, elastic-plastic material response and material failure. No computational model at present contains all of the necessary physics. However, we have

used several powerful computer codes with numerical diffraction and scattering models to extend our understanding of the initiation of laser damage.[13] In combination with carefully designed experiments, modeling can identify significant physical effects and scaling behavior.

First, we discuss several important physical effects accompanying laser interaction with metallic surface contaminants. Comparing the results of experiment and modeling, we address the following questions. What difference does it make if the contaminant is on the entrance or exit surface? What is the connection between plasma generation and damage? What is the effect of the surrounding environment? We then discuss damage initiation at subsurface absorbing nanoparticles embedded by the finishing process. Finally, we point out the danger posed by even nonabsorbing bulk defects.

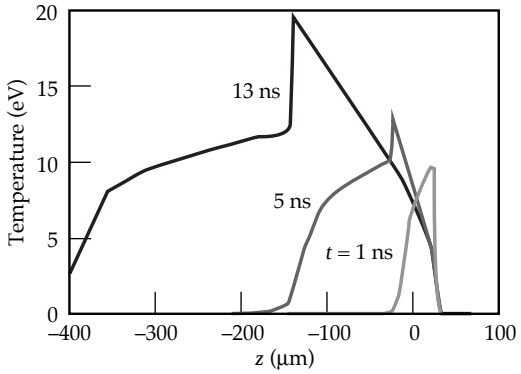

FIGURE 12. Temperature resulting from absorbing front-surface metallic particle on fused silica in air (8.5-ns pulse on 1-μm-thick Al). Air interface at $z = 0$. Air (to left of expanding metallic plasma) is heated by absorption of ultraviolet radiation from plasma. (70-00-0499-0971pb01)

Surface Contaminants

Optical surfaces can be contaminated by small particles, say from tens of nanometers to hundreds of micrometers in size. These arise, for example, from dust, condensation, or debris from light interaction with chamber walls and targets. Various types, sizes, and shapes of contaminant have been studied. The simulations presented here refer to artificial "particles" deposited onto a silica substrate. These 1-μm-thick particles of C, Al, or Ti were sputter-deposited through a mask and were either round or square. Damage initiation experiments were carried out in the 3ω Laser Damage group labs and at the OSL.

For metallic particles, laser light is absorbed in a thin skin depth leading to strong heating and plasma formation. The temperature of the resulting plasma can be as high as 20eV resulting in multiple ionization of the material. Such a hot plasma is a strong radiator of UV and soft x rays. In this case, radiation transport dominates thermal conduction as a means of transporting energy. This radiation is strongly absorbed in any surrounding air, causing heating and further ionization. In this case, the ionization front in the air can expand supersonically. Figure 12 shows our results for irradiating a front-surface absorber in air. The hot "shoulder" seen at the left at late times is air that has been heated through absorption of UV radiation. UV emission from the plasma can also be absorbed in the substrate, creating color centers that increase absorption seen by subsequent pulses.[14] The strongly localized energy deposited in the substrate produces strong shock waves that can cause mechanical damage. Finally, the plasma radiation can induce electronic defects in the glass that permanently change its characteristics and decrease the damage threshold for subsequent pulses.

Laser damage usually is easier to induce on the exit surface. Conventional wisdom points to Fresnel reflection and interference inside the material as the source of this asymmetry.[15] However, the predicted ratio of thresholds does not always hold, and this effect should vanish for antireflection-coated optics. Another difference between contaminated entrance and exit surfaces is that with absorption on the entrance surface, the plasma formed expands and shields the particle from the incoming laser light; that is, further laser energy is absorbed in the plasma itself. Consequently, the pressure pulse launched into the substrate is on the order of 10 kbar. With the absorber on the exit surface, however, the plasma is formed at the interface of two solid materials and confined. The high density of the plasma means higher heat capacity, lower temperature, and much higher pressures (say, 60 kbar) leading to a lower laser damage threshold. Figure 13 compares these two cases.

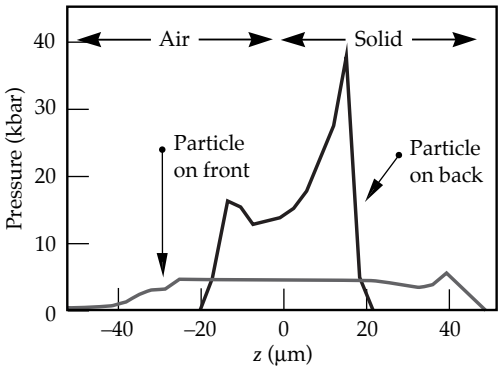

FIGURE 13. Pressure profiles resulting from front- or rear-surface contaminants are different due to plasma confinement for the rear-surface case. Higher temperatures were also calculated for the rear-surface case.
(70-00-0499-0972pb01)

Subsurface Absorbing Nanoparticles

Experimental observation shows that micropit damage spots appear near the laser damage threshold, particularly on the exit side of nominally clean fused silica samples (see Figure 14). All micropits have comparable sizes, with depth comparable to the width. Pits tend to be elongated, and cracks open preferentially normal to the electric field polarization direction.

It is natural to think that such pits are initiated by subwavelength particulate absorbers in the subsurface layer. Such an absorber might be a small contaminant particle, for example, due to the polishing process. Polishing a brittle surface can result in a thin layer of nearly invisible mechanical damage (microcracks). These cracks can serve as damage initiation centers, particularly if some absorbing material is trapped in them. This appears to be the case for certain ceria-containing polishing compounds. Because ceria is strongly absorbing at 3ω, we will consider ceria nanoparticles here. Heating the material around the absorber can result in further absorption increase, thermal explosion, material ejection, and crater formation.

Heating

The absorption cross section σ for a particle small compared to an optical wavelength is given in Refs. 16 and 17. The fraction of light incident on the geometric cross section that is absorbed is given by $\alpha = \sigma/\pi a^2$. Starting from a very small radius a, α will initially grow faster than linearly with a, and then, if the absorber's dielectric coefficient is of large magnitude, tends to saturate at large particle size. Because of diffraction, this absorption fraction can actually be larger than unity, i.e., more laser energy is absorbed than that intercepted by the particle's geometric cross section.

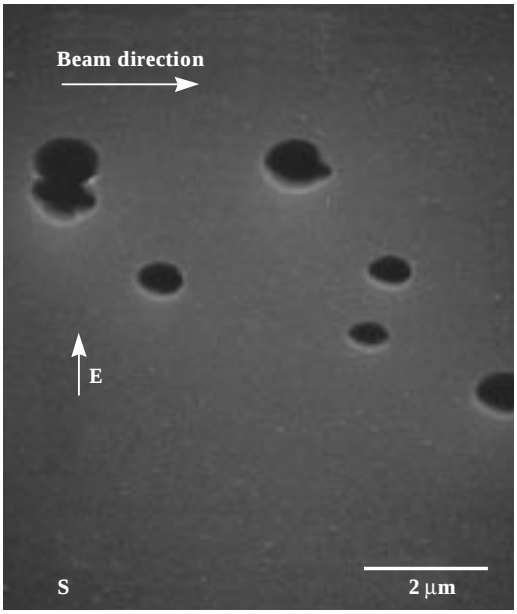

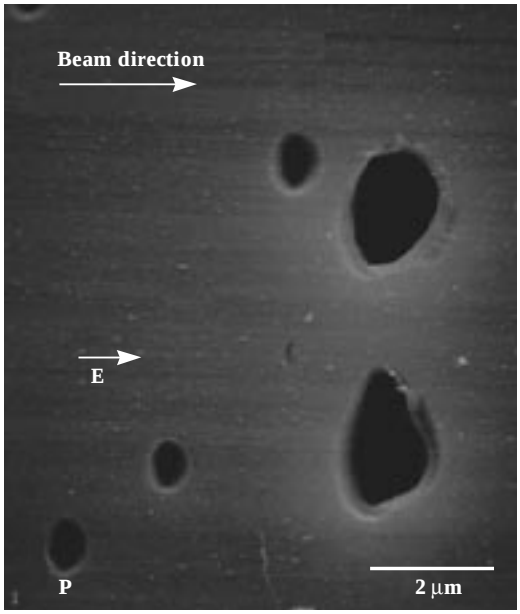

FIGURE 14. Micropit laser-induced damage observed on initially pit-free fused silica surface shows characteristic subwavelength size and orientation with respect to polarization of laser electric field (courtesy of F. Génin).
(70-00-0499-0973pb01)

The size of the absorber is also typically much smaller than a thermal diffusion length. This simplifies treatment of the temperature in the surrounding material, which can be treated as stationary. In Figure 15 we present the peak temperature T_0 for a ceria particle with refractive index $n = 2 + 0.2i$. The light intensity was assumed to be 3 GW/cm^2, and the pulse duration was taken as 3 ns. The thermal conductivity was taken as 0.014 W/cm K. In the figure, $ka = 0.5$ corresponds to a ceria particle with radius about 28 nm. Here $k = 2\pi/\lambda$ is the wave number of the light, and a is the radius of the particle. The peak temperature grows as the square of the particle size divided by the wavelength for small particles. This result demonstrates why the NIF third-harmonic light is more dangerous than the fundamental. The absorption efficiency depends on the particle size measured in wavelengths, so it is effectively three times as large at the third harmonic.

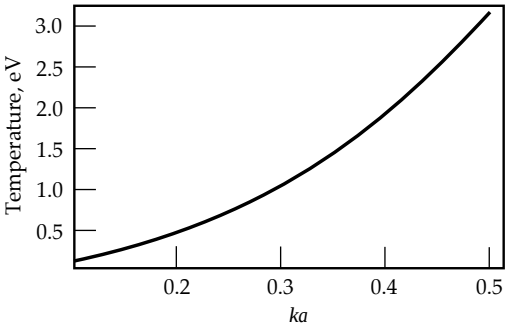

FIGURE 15. Calculated peak temperature increases at a ceria particle of radius a embedded in fused silica. Laser fluence was 9 J/cm^2 at 3ω. (70-00-0499-0974pb01)

Thermoelastic Stress

When the temperature distribution is known, the thermoelastic stresses can be calculated.[18] For example, Figure 16 shows the **xx** component of stress for a spherical ceria particle embedded in fused silica. The peak temperature was assumed to be 1000 K, and the coordinates are given in terms of the particle radius. Notice that the radial stress (equatorial in the figure) is compressive while the tangential or hoop stress (at the poles) is tensile. For an infinite medium, the stress distribution is symmetric as shown. For a near-surface particle, the presence of the free surface modifies the distribution, and material failure most likely occurs initially around the equator of the particle (the "pole" is directed toward the surface).

Glass Damage

The DYNA2D time-dependent mechanical response code[13] was used to model the damage to fused silica due to heating of a near-surface subwavelength ceria particle. A tensor damage model was used to describe the mechanical damage of brittle material. For low loading, elastic waves can propagate. At higher loads, plastic deformation and tensile and compressive failure can occur. The fact that material strength is larger for loads applied only a short time is taken into account using parameters determined from experiments on high-velocity projectile impacts on glass.

We considered a ceria particle embedded in glass. It was assumed that the glass outside the particle is nonabsorbing. The ceria particle was described with the same type of damage model as the glass, but with different parameters.

In the runs presented below, we consider 100-nm-radius particles at distances of 300 nm and 150 nm from the surface. Energy was deposited at a constant rate for 3 ns, which corresponds to a laser fluence of 10 J/cm^2. Figure 17 shows the damage distribution in ceria and glass for particles placed 300 nm under the surface at 1, 2, and 2.5 ns, respectively. The figure indicates the

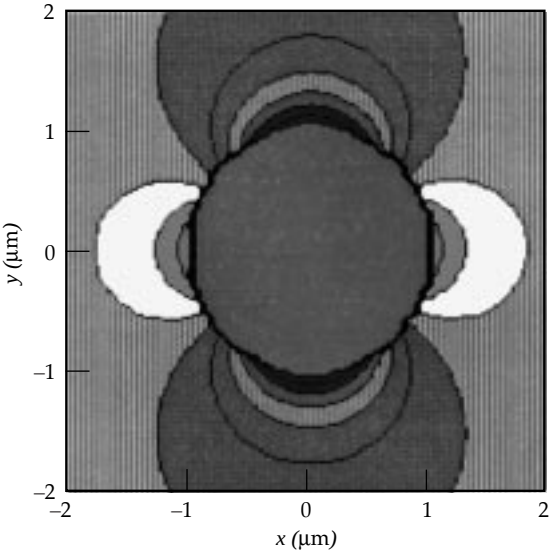

FIGURE 16. Variation of **xx** component of stress near embedded ceria particle in silica. Peak temperature is 1000 K and drops off as $1/r$ outside particle. Radial stress is compressive and hoop stress is tensile at particle substrate interface. (70-00-0499-0975pb01)

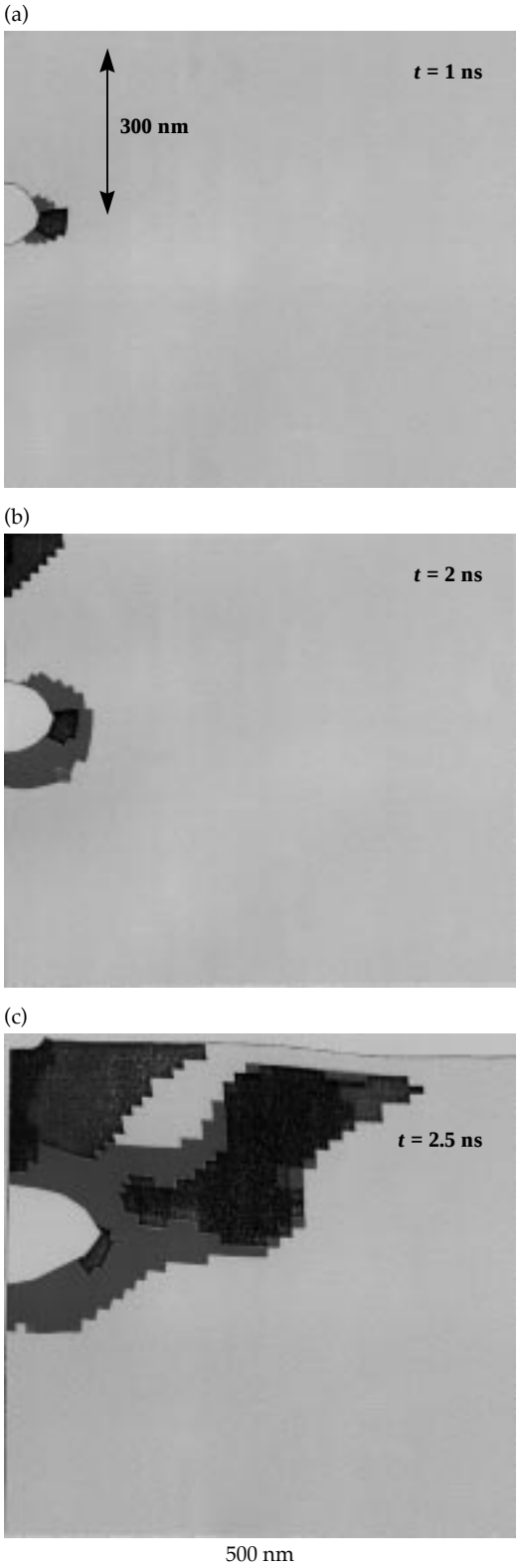

FIGURE 17. Growth of material damage in fused silica due to buried 100-nm ceria particle 300 nm below the surface. Damage initiates near the particle equator and grows to the surface to form a conical region (a) after 1-ns irradiation, (b) 2-ns, (c) 2.5-ns. The material inside the conical region is eventually completely crushed and ejected (calculation by D. Faux). (70-00-0499-0976pb01)

amount of damaged material. Because thermal expansion in ceria is much larger than that of fused silica (130×10^{-7} K^{-1} vs 7×10^{-7} K^{-1}), thermal expansion generates the initial stresses and damage in the surrounding material. Simultaneously, the shock reaches the free surface and reflects back, generating tensile stresses that easily damage the material. As noted above, because of the free surface, fracture propagates from the equator toward the free surface as additional material fails as stresses are redistributed. The damaged region forms a characteristic conical shape. At the closest and farthest parts of the region, the particle stresses are mainly compressive and initially do not damage the material. Later increases in pressure and arrival of the reflected wave crush most of the material within the cone. All mechanical resistance to shear is destroyed within the cone. The crushed material is finally ejected, forming a conical pit similar to that observed in experiments. The velocity of ejection is not high, only 150 to 200 m/s. It takes a comparatively long time to evacuate the pits. If the completely damaged material is taken as the eventual pit boundary, the estimated pit diameter is about 800 nm and the depth about 400 nm.

This model assumed fixed absorption and does not take into account thermal explosion, i.e., growth of absorption with contaminant heating. We estimate this effect in the next section.

Thermal Explosion

When the temperature around the inclusion reaches a critical value, a thermal explosion takes place.[19,20] This involves the rapid expansion of the heated region into the glass, which is then ionized. It occurs because the plasma produced by the initially absorbed light radiates UV, which is strongly absorbed in the matrix resulting in heating and an increase in the absorption coefficient of the glass. The situation is very similar to laser-supported ionization waves,[20,21] the main difference being that absorption occurs in a volume instead of just at a front.

Our analysis shows that the radius of the absorbing region tends to grow exponentially: $a = a(0) \exp G$, where the growth factor G is given by

$$G = 10\frac{F\omega}{n_e I_0 c}\,\mathrm{Im}\frac{1}{\varepsilon+2} \tag{5}$$

For absorption at 3ω, solid-state density electron n_e, ionization potential I_0 of 10 eV, fluence F of 10 J/cm^2, and a scattering rate 0.5 of the optical frequency, the growth factor G is about 10. The plasma ball will rapidly grow to a size comparable to a wavelength, after which exponential growth ceases. For the parameters used above, this final radius a is about 500 nm. Any nanoparticle strong absorber will initiate damage of at least this size.

Nonabsorbing Bulk Defects

The danger posed by absorbing defects in a transparent substrate has long been recognized and understood.[22] Such defects absorb energy, and they heat and expand, thereby thermally and mechanically stressing the surrounding material. It is also known that pure diffractive effects (e.g., clipping at the pinhole) in high-power laser systems can lead to laser-induced damage by causing intensity modulations that seed nonlinear self-focusing.[23,24] In this case, nonlinear refraction increases the local beam intensity level above the damage threshold.

For high-power laser systems, intensity modulations due to purely transparent defects may be capable of inducing damage without invoking any nonlinear effects. Both negative index defects (e.g., voids) and positive index defects (e.g., high-refractive-index inclusion) scatter light strongly, causing strong localized intensity modulation. High-refractive-index inclusions are especially dangerous since they act like efficient focusing lenses.

The situation of interest here is in the borderline area of wave optics and geometric optics. Very small defects (size comparable to a wavelength) with refractive index not very much different from that of the surrounding material can be treated by perturbative methods (Born approximation, WKB method, etc.) or treated by paraxial wave propagation. In the present case, we are interested in defects up to many wavelengths in size with very large differences in refractive index (e.g., –0.5 for a void up to +0.6 for a pure zirconia inclusion). This situation cannot be treated by paraxial optics since it involves strong reflections including total internal reflections inside an inclusion.

The vector theory of electromagnetic scattering was worked out by Mie; it is described in the classic book of Van de Hulst.[17] To be definite here, we choose to model spherical defects for which the solution can be calculated in a convenient form. In the case of larger (compared to wavelength) spheres, it is adequate to use the scalar approximation familiar from spherical scattering in the Schroedinger equation. That is, we wish to solve the scalar wave equation

$$\nabla^2 E + k_0^2 \eta(r)^2 E = 0 \tag{6}$$

where k_0 is the free space wave number $2\pi/\lambda$, and $\eta(r)$ is the spatially dependent refractive index. The refractive index is assumed to have the value η_1 inside a sphere of radius a, and the value η_2 outside this sphere. For convenience, we define the material wave numbers $k_{1,2} = k_0\,\eta_{1,2}$. Then, the solution can be written as a superposition of spherical waves of the form

$$E = \sum_{l=0}^{\infty}(2l+1)i^l \exp(i\delta_l) \times\left[j_l(k_2 r)\cos(\delta_l) - n_l(k_2 r)\sin(\delta_l)\right] \times P_l(\cos\theta) \tag{7}$$

Here j_l and n_l are spherical Bessel functions and P_l is a Legendre polynomial. The effect of the scatterer centered at $r = 0$ is given by the phase shifts δ_l, which vanish identically for no scatterer. The phase shifts are determined from a transcendental eigenvalue equation

$$\tan(\delta_l) = \frac{k_2 j_l'(k_2 a) - \gamma_l j_l(k_2 a)}{k_2 n_l'(k_2 a) - \gamma_l n_l(k_2 a)} \tag{8}$$

where

$$\gamma_l = \frac{k_l j_l'(k_l a)}{j_l(k_l a)} \tag{9}$$

and the primes denote differentiation with respect to argument. Although there are an infinite number of terms in the summation in Eq. 7, the number of partial wave phase shifts δ_l appreciably affected by the scattering is proportional to the size of the scatterer, i.e., roughly equal to ka. This is why it is computationally difficult to treat very large defects.

The calculations reported here are for small defects (wavelength scale and less) since these are most likely to occur. The intensifications important for damage initiation only become larger and persist over longer distances for larger defects. On the other hand, spherical defects probably exhibit the largest magnitude effect, especially for large refractive index inclusions. Actual defects need not be perfectly spherical, of course. Our results serve to point out the large intensifications, thus the serious consequences, which can result from transparent defects.

Voids

The distribution of intensity around a typical small spherical void (refractive index unity) in fused silica is shown in Figure 18. A plane wave of intensity unity is incident from above. Because the refractive index in the void is lower than that of fused silica, the void acts like a thick diverging lens. From a geometric optics picture, light rays are bent strongly away from the axis, leaving a "shadow" region behind the void. It is the intensity modulations on the edge of this shadow that concern us here. Intensity maxima of twice the incident intensity occur in the vicinity of the void. Further away, these maxima tend to die out. These modulations die out more slowly for larger voids (over a distance comparable with the Rayleigh range ka^2).

Inclusions

Defects with larger refractive index than the surrounding material are more dangerous since they act as concentrating lenses. These are not simple lenses, of course, because they are "thick," i.e., there is a large variation in optical path length over the incoming beam. Consider a spherical inclusion of radius a. The phase variation experienced by straight-ahead rays passing through the sphere is given by

$$\Delta\phi = 2Ka(\Delta n / n)[1 \pm (x / a)^2]^{1/2} \qquad (10)$$

at transverse position $x < a$. Here $\Delta n/n$ is the relative change in refractive index. Expanding the square root yields a simple estimate for the effective focal length as $a/(2\Delta n/n)$. This estimate is reasonably borne out by the wave-optical calculations, especially in that the focal length is proportional to the size of the sphere. The full calculation has to be carried out, however, to determine the intensity at the (aberrated) focus.

The intensification factor can be large, even when the change in refractive index is small. For example, the peak axial intensity (in units of the input intensity) downstream from a 4-μm sphere of index 1.51 in a silica ($n = 1.5$) substrate is about 1.5. A modest increase in refractive index of the inclusion to 1.6 increases the maximum intensity to 10 times the initial intensity.

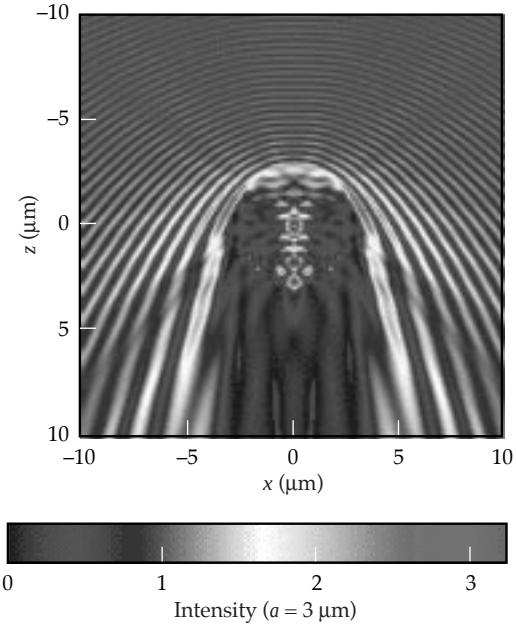

FIGURE 18. Distribution of intensity in vicinity of small spherical void in glass. Light incident from top. Note shadow region behind void and intensity modulations. (70-00-0499-0977pb01)

For a high-index inclusion, e.g., ZrO_2, a refractory used in fabrication of fused silica, the intensification is nearly 1000 (Figure 19). Bulk inclusions of high refractive index are thus expected to lead to damage even though they are unlikely to be perfect spheres. Because of the high vulnerability of surfaces, bulk damage produced by inclusions may be accompanied by associated exit surface damage.

Conclusions

In this paper, we have discussed models that describe two of the ways in which the NIF beam can interact adversely with laser components. These interactions can lead to pinhole closure in the spatial filters and laser-induced damage to optical elements such as lenses. We have discussed a complex model for 4-leaf pinholes and a simple model for pinholes in general, including the cone design. The models have been tested via data taken on OSL and Beamlet and appear to be adequate to make projections for NIF. For the description of laser-induced damage, our modeling has demonstrated the importance of very small absorbing particles as well as nonabsorbing particles in initiating the damage. We expect that such laser-interaction modeling, which involves a number of areas of physics and extensive numerical codes, will continue to contribute to the development of advanced laser technology.

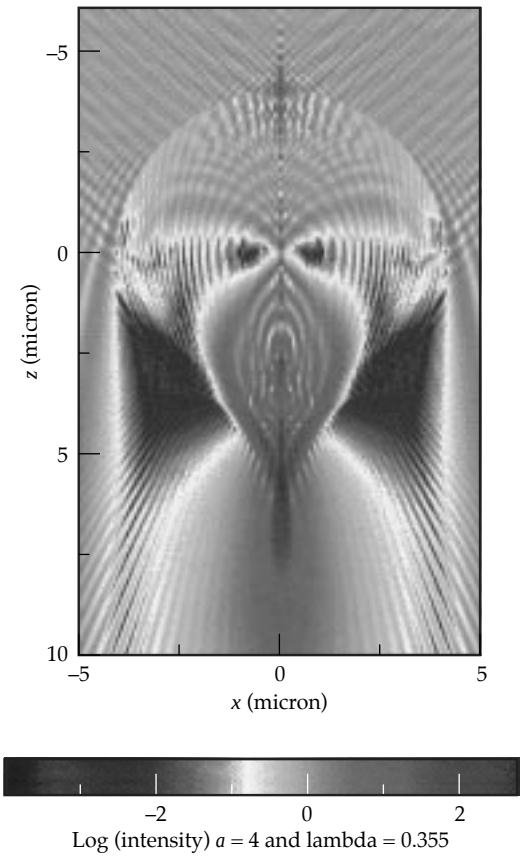

FIGURE 19. Light intensification near zirconia sphere (n = 2.1) in fused silica. Laser incident from top. (70-00-0499-0978pb01)

Acknowledgments

It is a pleasure to acknowledge the contributions of our colleagues to the work presented here. These colleagues include J. M. Auerbach, K. G. Estabrook, D. R. Faux, F. Y. Génin, M. R. Kozlowski, D. Milam, J. E. Murray, A. M. Rubenchik, S. Schwartz, and L. M. Sheehan.

Notes and References

1. J. T. Hunt, J. A. Glaze, W. W. Simmons, and P. A. Renard, *Appl. Opt.* **17**, 2053–2057 (1978).
2. See, e.g., J. T. Hunt, K. Manes, P. A. Reynard, *Appl. Opt.* **32**, 5973–82 (1993); for assessments for the 1ω chain, see M. D. Feit, C. C. Widmayer, W. H. Williams, R. A. Sacks, P. A. Renard, and M. A. Henesian, "NIF's assessment of the optical damage threat for flat in time pulses," and M. D. Feit, W. H. Williams, C. C. Widmayer, R. A. Sacks, and P. A. Renard, "Assessment of the damage threat for the two baseline ICF shaped temporal pulses," both in *NIF Laser System Performance Ratings*, Lawrence Livermore National Laboratory, Livermore, CA, UCRL-ID-131115 (July 1, 1998).
3. M. R. Kozlowski, R. P. Mouser, S. M. Maricle, P. J. Wegner, and T. L. Weiland, "Laser damage performance of fused silica optical components measured on the Beamlet laser at 351 nm," p. 428; S. Schwartz, M. D. Feit, M. R. Kozlowski, and R. P. Mouser, "Current 3ω large optic test procedures and data analysis for the quality assurance of National Ignition Facility optics," p. 314; M. D. Feit, A. M. Rubenchik, M. R. Kozlowski, F. Y. Génin, S. Schwartz, and L. M. Sheehan, "Extrapolation of damage test data to predict performance of large-area NIF optics at 355 nm," p. 226; all in *SPIE* **3578**: XXX Annual Symposium on Optical Materials for High Power Lasers, Boulder, CO, Sept. 28–Oct 1, 1998.
4. J. M. Auerbach, N. C. Holmes, J. T. Hunt, and G. J. Linford, *Appl. Opt.* **18**, 2495–2499 (1979).
5. P. M. Celliers et al., "Spatial filter pinhole for high-energy pulsed lasers," *Appl. Opt.* **37**, 2371–78 (1998).

6. J. E. Murray, D. Milam, C. D. Boley, and K. G. Estabrook, "Spatial filter pinhole development for the National Ignition Facility," in preparation.
7. D. Milam et al., "Pinhole Closure Measurements," Third Annual International Conf. on Solid State Lasers for Application to Inertial Confinement Fusion, Monterey, CA, June 7–12 (1998).
8. C. D. Boley, K. G. Estabrook, J. M. Auerbach, M. D. Feit, and A. M. Rubenchik, "Modeling of Laser Knife-Edge Experiments," Third Annual International Conf. on Solid State Lasers for Application to Inertial Confinement Fusion, Monterey, CA, June 7–12 (1998).
9. G. B. Zimmerman and W. L. Kruer, *Comments in Plasma Physics and Controlled Fusion* **2**, 51–61 (1975).
10. J. A. Harte, W. E. Alley, D. S. Bailey, J. L. Eddleman, and G. B. Zimmerman, *ICF Quarterly Report* **6**(4), 150–164, Lawrence Livermore National Laboratory, Livermore, CA, UCRL-LR-105821-96-4 (1997).
11. M. K. Prasad et al., *Phys. Fluids* **8**, 1569–1575 (1992).
12. J. M. Auerbach, Lawrence Livermore National Laboratory, Livermore, CA, internal communication (1998).
13. Laser absorption, ionization, and hydrodynamics were modeled with the HYADES code; cf. J. T. Larsen, "HYADES—A Radiation Hydrodynamics Code for Dense Plasma Studies," in *Radiative Properties of Hot Dense Matter*, edited by W. Goldstein, C. Hooper, J. Gauthier, J. Seely, and R. Lee (World Scientific, Singapore, 1991). Mechanical strength was modeled with Lawrence Livermore National Laboratory's DYNA code; cf. R. G. Whirley, B. E. Engelmann, and J. O. Hallquist, *DYNA2D—A Nonlinear, Explicit, Two-Dimensional Finite Element Code for Solid Mechanics User Manual*, Lawrence Livermore National Laboratory, Livermore, CA, UCRL-MA-110630 (1992).
14. A. P. Gagarin, L. B. Glebov, and V. G. Dokuchaev, *Kvant. Electron.* **4**, 1996 (1977); English translation in *Sov. J. Quant. Electr.* **7**, 1136 (1977).
15. N. L. Boling, M. D. Crisp, G. Dube, *Appl. Opt.* **12**, 650–60, (1973).
16. L. D. Landau and E. M. Lifshitz, *Electrodynamics of Continuous Media* (Pergamon Press, New York, 1960).
17. H. van de Hulst, *Light Scattering by Small Particles* (Dover Publications, New York, 1981).
18. A. P. Boresi, *Elasticity in Engineering Mechanics* (Prentice Hall, New Jersey, 1965).
19. M. F. Koldunov, A. A. Manenkov, I. L. Pokotilo, Sov. *J. Quant. Electr.* **18**, 345 (1988).
20. S. I. Anisimov and V. A. Khokhlov, *Instabilities in Laser–Matter Interaction* (CRC Press, Boca Raton, Florida, 1995).
21. M. von Allmen and A. Blatter, *Laser Beam Interactions with Materials* (Springer, Berlin, 1994).
22. See, e.g., "Modeling laser damage caused by platinum inclusions in laser glass," J. H. Pitts, *Laser Induced Damage in Optical Materials: 1985*, Boulder Damage Symposium, *NBS Special Publication 746* (1986).
23. J. A. Fleck, Jr., and C. Layne, *Appl. Phys. Lett.* **22**, 467–9 (1973).
24. N. B. Baranova, N. E. Bykovskii, B. Ya. Zel'dovich, and Yu. V. Senatskii, *Kvant. Electr.* **1**, 2435–49 (1974), translated in *Sov. J. Quant. Electr.* **4**, 1354–61 (1975).